This is a preprint, the final version is subject to change, of the American Mineralogist (MSA)
Cite as Authors (Year) Title. American Mineralogist, in press.
(DOI will not work until issue is live.) DOI: http://dx.doi.org/10.2138/am-2016-5533

Revision 1

Elasticity and Phase Transformation at High Pressure in Coesite from Experiments and First-Principles Calculations

Ting Chen[a], Xuebing Wang[a], Xintong Qi[a], Maining Ma[b], Zhishuang Xu[b], and Baosheng Li[c]

[a] *Department of Geosciences, Stony Brook University, Stony Brook, NY 11794, USA*
[b] *University of Chinese Academy of Sciences, Beijing 100049, China*
[c] *Mineral Physics Institute, Stony Brook University, Stony Brook, NY 11794, USA*

Abstract

The crystal structure and equation of state of coesite (space group $C2/c$) and its high pressure polymorph coesite-II (space group $P2_1/n$) under pressure have been studied using X-ray powder diffraction in a diamond anvil cell (DAC) up to 31 GPa at room temperature and first-principles calculations at 0 K up to 45 GPa. New diffraction peaks appear above 20 GPa, indicating the formation of coesite-II structure. The calculated enthalpies provide theoretical support for the pressure-induced phase transformation from coesite to coesite-II at ~21.4 GPa. Compared with coesite, the coesite-II structure is characterized by a 'doubled' *b*-axis and the breakdown of the linear Si1-O1-Si1 angle in coesite into two distinct angles - one is ~176°, close to linear, whereas the other decreases by 22° to 158°. Coesite is very anisotropic with the *a*-axis the shortest and twice more compressible than the *b*- and *c*-axis. By comparison, coesite-II is not so anisotropic with similar compressibilities in its *a*-, *b*-, and *c*-axis. As analyzed by a third-order Eulerian finite strain equation of state, the bulk modulus of coesite at 21.4 GPa is 182.3GPa, and that of coesite-II is 140.8 GPa, indicating that coesite-II is much more compressible than coesite. The existence of coesite-II in the coldest subduction zone will change the elasticity and anisotropic properties of the subducting materials dramatically.

Key Words: Coesite; phase transition; diamond anvil cell; first-principles calculation

Introduction

Coesite is a high pressure polymorph of quartz with the monoclinic structure and space group *C*2/*c*. It is thermodynamically stable at pressures and temperatures above 2.5 GPa and 500 °C (Akaogi and Navrotsky, 1984; Akaogi et al., 1995). Natural coesite has been discovered in meteorite craters and metamorphic rocks in subduction or collision zones, and used as a pressure marker for these events (e.g. Sobolev et al., 2000). The mid-ocean ridge basalt (MORB) is believed to contain an appreciable amount of SiO_2 (Ricard et al., 2005; Irifune and Tsuchiya, 2007; Stixrude and Lithgow-Bertelloni, 2012), and it has been proposed as a main candidate to explain the seismic observed X-discontinuity in the depth range 250-350 km (Chen et al., 2015; Williams and Revenaugh, 2005; Schmerr et al., 2013). Given the importance in these geological processes, it is of particular significance to understand the thermodynamics and elastic properties of coesite under pressure and/or temperature conditions.

Crystal structure studies show that coesite is a framework silicate with the Si atom coordinated with four oxygens (Fig. 1). The SiO_2 tetrahedra in coesite form four-membered rings by corner sharing, which then build up the 'double-crankshaft' chain running parallel to the *c*-axis of the unit cell. There are eight distinct Si-O bonds, and five distinct Si-O-Si angles in coesite structure, with a linear Si1-O1-Si1 angle. Static compression studies showed that these bonds and angles decrease under pressure, with the smaller angles and shorter bonds undergoing more compression than larger/longer ones, and the Si1-O1-Si1 remains linear due to the requirement of the symmetry (Levien and Prewitt, 1981). Coesite has 16 units of SiO_2 in a unit cell, with almost equal *a*- and *c*-axis, and β close to 120° at room conditions, which resembles that of a hexagonal structure.

48 The behavior of SiO_2 under pressure has long been of interest to geoscience and material
49 science due to its abundance in Earth crust and mantle, and its relative simple chemistry but rich
50 polymorphism under elevated pressure and/or temperature conditions, which could help to
51 understand the properties of silicate tetrahedra under pressure. It has been shown that under
52 pressure, the *a*-axis of coesite is much more compressible than *c*-axis, whose compressibility is
53 close to that of *b*-axis; and the β angle becomes larger with increasing pressure (Levien and
54 Prewitt, 1981; Angel et al., 2001), indicating strong anisotropic compression of its structure. The
55 elastic properties of coesite have been found to be anomalous under pressure by several studies.
56 For example, Angel et al. (2001) studied the compressional behavior of coesite up to 9.6 GPa
57 using single crystal X-ray diffraction and reported an unusual positive K_{T0}'' which they attributed
58 to the unusual compression of the *c*-axis. Our recent study (Chen et al., 2015) showed that the
59 shear wave velocity of coesite undergoes anomalous softening and decreases with increasing
60 pressure within 0-12.6 GPa. The anomalous behavior of the shear wave velocity and shear
61 modulus may be a precursor to the pressure-induced phase transition or amorphization with
62 further pressure increase (e.g., Karki et al., 1997a, 1997b; Carpenter and Salje, 1998). The
63 softening in shear wave velocity of coesite is in accordance with a density-functional theory
64 calculation by Kimizuka et al. (2008), which reported that the shear elastic constant C_{44} of
65 coesite decreases with increasing pressure. Moreover, previous Raman spectroscopy (Hemley,
66 1987) and X-ray diffraction (Hemley et al., 1988) studies all suggest that coesite transforms to a
67 metastable high pressure phase at 22-25 GPa at room temperature, and then becomes amorphous
68 at higher pressure between 25-35 GPa. By contrast, a more recent Raman spectroscopy study in
69 diamond anvil cell up to 51 GPa by Černok et al. (2014a) reported two phase transitions at ~23
70 GPa and ~35 GPa; however, instead of becoming amorphous, coesite was found to remain as a

71 crystalline phase up to the highest experimental pressure 51 GPa, which is consistent with a more
72 recent study by Hu et al. (2015) using single-crystal synchrotron X-ray diffraction and first-
73 principles calculations.

74 However, in spite of these extensive previous experimental and theoretical studies,
75 additional research on the coesite to coesite-II phase transition is still needed. In this study, we
76 conducted a high-pressure angle dispersive X-ray diffraction study on powdered coesite sample
77 in a diamond anvil cell (DAC) up to 31 GPa, and determined the cell parameters and unit cell
78 volumes under pressure. In addition to these experiments, we performed first-principles
79 calculations on coesite and its high-pressure polymorphs (stishovite and coesite-II) up to 45 GPa
80 to investigate their relative stability, compressibilities, as well as structural change pathways
81 under pressure.

82 **Experiments and Theoretical Calculations**

83 The coesite sample (K1005) used in the current experiment was synthesized at 6 GPa
84 950°C for 2.5 hours in a 1000-ton uniaxial split-cylinder apparatus (USCA-1000) in the High
85 Pressure Laboratory at Stony Brook University using silicon dioxide powder as the starting
86 material. The recovered sample was determined to be pure coesite by powder X-ray diffraction.
87 In-situ high-pressure synchrotron X-ray diffraction experiments starting with this coesite powder
88 were performed in a diamond anvil cell up to 31 GPa at beamline X17C of National Synchrotron
89 Light Source (NSLS) in Brookhaven National Laboratory (BNL). Both of the opposing diamond
90 anvils used in the current experiments have a culet size of 350 μm. The samples were dried at
91 373 K for >2 hrs in the oven before loading into the hole drilled in the center of a T301 stainless
92 steel gasket, which was pre-indented to 70 μm with an initial thickness of 267 μm. The

fluorescence of two ruby pieces loaded in the sample chamber along with the coesite sample was used for pressure measurement (Mao et al., 1986). A mixture of methanol-ethanol with volume ratio 4:1 was used as the pressure medium, which provides hydrostatic conditions up to ~10 GPa (Klotz et al., 2009). X-ray diffraction patterns were collected during pressurization with a typical pressure increment interval of 1-2 GPa and exposure time 1600-1800 s using a Rayonix165 CCD detector. We integrated the two-dimensional X-ray diffraction images as a function of 2θ using software package Fit2D (Hammersley et al., 1996), followed by unit cell parameters refinement using Le Bail method with the GSAS/EXPGUI program (Toby, 2001; Larson and Von Dreele, 2004).

The first-principles calculations using density functional theory (DFT) were performed within a generalized gradients approximation (GGA) framework of PBE (Perdew et al., 1996) exchange correlation functions and local density approximation (LDA) of CA-PZ exchange correlations of Ceperley and Alder (1980) parameterized by Perdew and Zunger (1981) as implemented in the CASTEP package. All computations were performed using a primitive cell to obtain equilibrated structures and enthalpies for coesite, stishovite, and coesite-II under pressure with ultrasoft pseudopotentials of Si (Rc=1.8 a.u., $3s^2 3p^2$) and O (Rc=1.0 a.u., $2s^2 2p^4$). A combination of plane wave cut-off energy E_{cut}=800 eV (1250 eV for LDA calculations) and a 3×3×3 Monkhorst-Pack k-mesh (3×1×3 for coesite-II) was used with convergence criteria of 1×10^{-5} eV/atom in energy, 0.03 eV/A in force, and 0.05 GPa in pressure for both coesite and coesite-II structures. GGA calculations with higher plane wave cut-off energy of E_{cut}=1250 eV result in changes of 0.2%-1.6% in lattice parameters (*a*, *b*, *c*, *β*), while tests with higher k mesh indicate almost no difference in the resultant enthalpies. Compared with experimental data, the current GGA (LDA) results overestimate (underestimate) the lattice parameters of coesite by ~1.0%

(unit cell volume by 2.2%) because of underbinding (overbinding), zero-point motion and difference in temperature.

Results and discussions

1. Enthalpies of SiO_2 phases

The relative enthalpies of coesite, stishovite and coesite-II from GGA and LDA calculations are compared in Fig. 1 as a function of pressure. As indicated in Fig. 1, stishovite has lower enthalpy than coesite above ~8.5 GPa, and the difference grows larger with pressure to -0.3 eV/atom at 25 GPa. This indicates that, thermodynamically, it is the stable phase, consistent with that revealed in previous experiments (e.g., Zhang et al., 1996). However, the reconstructive phase transition from coesite to stishovite at lower temperatures is hindered due to the high kinetic barrier and the high pressure but low temperature condition, resulting in various metastable phases (e.g. Hemley, 1987; Černok et al., 2014a, 2014b; Hu et al, 2015). Above 25 GPa from GGA calculations, the coesite-II structure with space group $P2_1/n$ becomes thermodynamically more stable than coesite structure as suggested by the relatively low enthalpy, although the difference, ranging from -0.01 eV/atom at 30 GPa to -0.02 eV/atom at 45 GPa, is much smaller than that between coesite and stishovite. This provides theoretical support for the phase transition from $C2/c$ to $P2_1/n$ in coesite. Within 0-25 GPa, we note that, although coesite has been experimentally demonstrated to be more stable than coesite-II, the enthalpies of these two structures are almost the same in the pressure range 0-25 GPa and the relaxed equilibrium structure parameters (Table 1) are nearly identical, which in turn may have facilitated the transition from $C2/c$ coesite to $P2_1/n$ coesite-II at higher pressures. The relative enthalpy between coesite and coesite-II from LDA calculations is similar to that from GGA calculations except that

the pressure of the phase transition occurs at lower pressure, which is consistent with previous finding that the LDA calculations underestimate the transition pressure in comparison with GGA (e.g. Oganov and Ono, 2004).

2. Pressure induced phase transition and equation of state

Selected experimental X-ray diffraction patterns at elevated pressures are shown in Fig. 2. For comparison, the theoretical diffraction patterns for coesite at 25 GPa and for coesite-II at 25 GPa and 30 GPa are also included. As seen in Fig. 2, no pronounced changes in the diffraction pattern were observed within the pressure range of 0-14 GPa, except for the anisotropic shifts in 2θ angles displayed by different diffraction peaks due to anisotropic compressions of crystal axes *a*, *b*, *c* which leads to an increased separation among the peaks grouped around 2θ~6.7-7° and 2θ~7.5-8°. At pressures above 14 GPa, the diffraction peaks become broader due to the solidification of the pressure medium. As a result, unambiguous indexing of individual peaks for phase identification becomes difficult. We notice that up to 25 GPa, although the theoretical diffraction patterns for coesite and coesite-II are very similar; the pattern for coesite-II at 30 GPa, however, clearly shows some characteristic peaks at 2θ~8.5° not overlapped with those of coesite which can help diagnose the transition (see theoretical diffraction patterns in Fig. 2). A closer examination indicates that, as circled in Fig. 2, there are indeed relatively small new peaks emerging in the experimental diffraction patterns above 20 GPa, which cannot be due to the coesite, instead, the positions of these new peaks correspond well to the diffraction peaks of (0 3 2) (-2 3 2) (2 2 0) (1 5 -2) [may also contain contributions from weaker (2 5 -1) (1 5 1)] as indicated by the arrows in the theoretical patterns for coesite-II. Another line of evidence for the

160 formation of coesite-II is that, the main peaks around 2θ ~7.5-8° shift to slightly higher angles
161 within 20-25 GPa followed by a visible slope change with increasing pressure; this is consistent
162 with the current finding that coesite-II has a higher compressibility than coesite (see next section
163 on compressibility).

164 The unit cell volume (for 16 SiO_2 units) for coesite obtained from the current DAC
165 experiments, together with those for coesite and coesite-II from the first-principles (GGA)
166 calculations, are given in Table 1 and plotted in Fig. 3. As stated above and clearly seen in Fig. 2,
167 due to the effect of the methanol-ethanol pressure medium in the DAC experiments (see also
168 Klotz et al., 2009), only the data obtained below 14 GPa are of adequate quality for reliable
169 lattice parameter refinement. For comparison, the results for these two structures from single-
170 crystal X-ray diffraction studies by Černok et al. (2014b) and Hu et al. (2015) are also plotted.
171 Since the original results for the unit cell volumes from GGA calculations are systematically
172 higher than experimental data, a closer comparison is thus accommodated by applying a
173 correction of -3.6 GPa to the GGA pressures listed in Table 1 by using unit cell volume at zero
174 pressure as the reference. The unit cell volumes of coesite from our DAC experiment are in
175 excellent agreement with those from Černok et al. (2014b) as well as those predicted by first-
176 principles calculations.

177 The volumes of coesite and coesite-II are indistinguishable at pressures below 20 GPa;
178 with further increase in pressure, the volume of coesite-II becomes smaller than that of coesite
179 and the difference increase from 1.1% at 21.4 GPa to 2.0% at 26.4 GPa. For coesite-II, available
180 experimental data are limited to two data points in each of the two recent studies by Černok et al.
181 (2014b) and Hu et al. (2015) at pressures below 35 GPa, and the equation of state of coesite-II
182 has not been evaluated in these previous studies. A comparison between the current DFT results

and those from Černok et al. (2014b) and Hu et al. (2015) reveals that the predicted values are in complete agreement with those from experiments below 35 GPa, above which the coesite-II structures were found to transform to a new structure as characterized by an accelerated decrease in the unit cell volume (for 16 SiO_2 units) in comparison with the predicted values from the first principles. According to Hu et al. (2015), this feature marks the transformation pathway from 4- to 5- to 6- coordination silicon during the transformation to the monoclinic post stishovite structure.

The current *P-V* data from DAC experiments were fitted using a weighted third-order Eulerian finite strain [hereafter referred to as Birch-Murnaghan] equation of state (Davies and Dziewonski, 1975) with the volume (V_0), bulk moduli (K_0) and its pressure derivative (K_0') at room condition as free parameters. The results are V_0 =547.1 Å^3, K_0 =106.2 GPa and K_0' =2.1 (Table 2). The data from GGA calculations were fitted to third-order Eulerian finite strain equations (Birch, 1978):

$$E(V) = E_0 + \frac{9V_0K_0}{16}\left\{\left[\left(\frac{V_0}{V}\right)^{2/3} - 1\right]^3 K_0' + \left[\left(\frac{V_0}{V}\right)^{2/3} - 1\right]^2 \left[6 - 4\left(\frac{V_0}{V}\right)^{2/3}\right]\right\}$$

, yielding K_0 =92.8 GPa and K_0' =3.6 for coesite. With a pressure correction of -3.6 GPa, the GGA results for coesite show good agreement with the data from experimental studies (see Fig. 3) and can be prescribed by an equation of state with V_0 =546.2 Å^3, K_0 =96.2 GPa and K_0' =4.3 (Table 2). And those for coesite-II at 21.4 GPa are $K_{21.4GPa}$ =140.8 GPa, $K_{21.4GPa}'$ =3.6 by fitting the data above 21.4 GPa to avoid influence of the different trend at low pressures. The unit cell volumes of coesite from the current experiments (547.1 Å^3) and DFT calculations (546.2 Å^3) compare well with the values of 546.80 Å^3 (Angel et al., 2001) and 546.46 Å^3 (Levien and

Prewitt, 1981) from single-crystal X-ray diffraction studies. Note that the K_0 from the current DFT calculations using equation of state approach is in excellent agreement with that obtained from single crystal elastic constants calculated by Kimizuka et al. (2008). The discrepancies in K_0 and K_0' between experiment and DFT calculations may result from the different pressure range as well as the well-known trade-off between K_T and K_T' in equation-of-state fit. It is worth noting that, according to Angel et al. (2001), the bulk modulus of coesite has a positive second order pressure derivative, thus, a higher K_0' is expected when fitting data from a wider pressure range using the same third order Birch-Murnaghan equation.

To compare with coesite-II at high pressures, we also calculated the bulk modulus at 21.4 GPa using the 3rd order Birch-Murnaghan equation (Birch, 1978) $K = (1+2f)^{5/2}K_0\left[1+\right.$ $\left.3K0'-5f-272(4-K0')f2,\ f=12V0V2/3-1\right.$, resulting in $K_{21.4GPa}$=182.3GPa for coesite. This value is much larger than that of coesite-II ($K_{21.4GPa}$=140.8 GPa), indicating that coesite-II is 23% more compressible than coesite. This observation provides strong support for the interpretation of the evolution of the X-ray diffraction patterns (Fig. 2) that the diffraction peaks shift to higher angles more rapidly after the phase transformation to coesite-II.

3. Crystal structure of coesite and coesite-II

Unit cell parameters of coesite and coesite-II from DFT calculations (Table 1) were fitted to a Birch-Murnaghan equation of state, and the axial bulk modulus of the two phases were obtained (Table 3). The K_a, K_b, and K_c from our DFT calculations are in good agreement with those of Černok et al. (2014b) with the largest difference (~9%) in K_a. And the K_c from our DAC experiments is lower than the other two results, which is probably caused by the different pressure range, as well as the trade-off in the equation of state fitting. The resultant axial

compressibilities for coesite at room pressure are 4.5×10^{-3} GPa^{-1}, 2.3×10^{-3} GPa^{-1}, and 1.9×10^{-3} GPa^{-1} for *a*-, *b*-, and *c*-axis, respectively from our DFT calculations, indicating strong anisotropy of its compression behavior with the *a*-axis about 96% and 137% more compressible than *b*- and *c*-axis, respectively. By comparison, those for coesite-II at 21.4 GPa are 2.4×10^{-3} GPa^{-1}, 2.6×10^{-3} GPa^{-1}, and 2.2×10^{-3} GPa^{-1} for *a*-, *b*-, and *c*-axis respectively. The compressibilities of the three axes are much closer in coesite-II, indicating that the compression in coesite-II structure is much less anisotropic at high pressure than coesite.

Despite the discrepancies in the axial compressibilities in Table 3, the evolution of the unit-cell parameters as a function of pressure for coesite and coesite-II from the current study are in good agreement with those from Černok et al. (2014b) (Fig. 4). Within ~21.4-26.4 GPa, the *b*- and *c*-axis undergo sharper decreases because of the phase transition, ranging from 0.9% at 21.4 GPa to 1.5% at 26.4 GPa for *b*-axis, and from 0.5% to 0.8% for *c*-axis; in contrast, the *a*-axis exhibits a negligibly small increase (Fig. 4). During compression, the β angle for coesite increases continuously up to the transition pressure at ~21.4 GPa for coesite, after which the β angle in coesite-II structure starts to decrease. On the other hand, the only two experimental data points at ~27 and 31 GPa from Černok et al. (2014b) seem to suggest an increase of the β angle. This discrepancy in β angle cannot be reconciled and more experimental data are still needed.

Based on the current DFT calculations, a detailed analysis was performed on the evolution of Si-O bond length and Si-O-Si angle under pressure. The results for the eight distinct Si-O bonds of coesite are shown in Fig. 5(a) (See also Supplement 1), together with the four Si-O bonds of coesite-II evolved from the shortest Si1-O1 in coesite. As seen in Fig. 5 for coesite, the shorter Si-O bonds are more compressible as evidenced by the steep slopes as a function of pressure, with the shortest Si1-O1 undergoing 8.5% shortening at 21.4 GPa. This result is

consistent with those reported in previous experimental (Černok et al., 2014b; Angel et al., 2003) and theoretical (Gibbs et al., 2000) studies. As a consequence, the Si1 tetrahedron is more compressible than Si2 tetrahedron, rendering a volume reduction of 7.3% and 5.8% at 21.4 GPa for Si1 and Si2 tetrahedron respectively. The Si1-O1 then evolves into four distinct lengths in coesite-II, with two of them following the trend in coesite and the other two showing 1.3% increase. Another characteristic feature of this transformation is that, the linear Si1-O1-Si1 angle, which is constrained to be 180° in coesite due to symmetry requirement, breaks down at ~21.4 GPa, resulting in two independent angles (Si2-O15-Si3 and Si5-O4-Si7) in coesite-II. One of the Si1-O1-Si1 evolved angles (Si2-O15-Si3) decreases by 22° to 158 °, while the other (Si5-O4-Si7) is ~176°, close to linear (Fig. 5b, Fig. 6). With further increase in pressure, the Si2-O15-Si3 in coesite-II undergoes a monotonic decrease while the Si5-O4-Si7 angle experiences relatively small change and remains close to linear. The distortion of the linear Si1-O1-Si1 angle results in the loss of mirror planes during the phase transition from coesite to coesite-II. Besides the changes in the angles and bonds related to the O1 atom in coesite, the Si1-O4-Si2 in coesite also undergoes considerable change and evolves into four angles in coesite-II, with two of them close to the original Si1-O4-Si2 (~146°), one increases to 164°, and the other decreases to 136°. These analyses shed insights into the atomistic pathways for the formation of coesite-II from a *b*-axis doubled coesite structure.

Implications

By analyzing the X-ray diffraction patterns from diamond anvil cell experiments on powdered coesite sample, combined with DFT calculations on coesite and its high pressure polymorphs coesite-II and stishovite, we studied the pressure-induced phase transformation from coesite to coesite-II and the elasticity of these two structures to garner better understanding on

their behavior under mantle pressures. The current data for coesite and coesite-II are in good agreement with those from previous studies (e.g. Černok et al., 2014b; Hu et al., 2015), that coesite-II is deemed a product in the transformation pathway from 4- to 5- to 6- coordinated structure of SiO_2. The bulk modulus of coesite and coesite-II are determined from DFT calculations, yielding $K_{21.4GPa}$=182.3GPa for coesite and $K_{21.4GPa}$=140.8 GPa for coesite-II. This indicates that under mantle pressures coesite-II is much more compressible than coesite and a decrease of the bulk sound velocity by ~12% is expected across the transition.

As of today, the structural change from coesite to coesite-II has only been observed at high pressure and room temperature conditions. It remains to be further investigated as to what temperature this structure transformation can persist at mantle pressures. For instance, a recently discovered new metastable phase of orthopyroxene has been found to exist at temperatures least up to 673 K (Zhang et al., 2014). Similarly, if coesite-II can exist at moderately low temperatures, then coesite-II might be considered as a metastable phase in cold subduction zones; the phase transition will change the elasticity as well as anisotropic properties of the subducted oceanic crust due to the dramatically different compressional behavior between coesite and coesite-II as well as the appreciable amount of SiO_2 in the MORB (Ricard et al., 2005; Irifune and Tsuchiya, 2007; Stixrude and Lithgow-Bertelloni, 2012). Considering ~14% of SiO_2 in the MORB mineralogy as suggested in Ricard et al. (2005), it will cause ~1.7% of bulk sound velocity change across the phase transformation from coesite to coesite-II, which should be detectable by seismic studies. The velocity decrease is even more significant when subducted sediments, which can contain up to ~20 wt% of SiO_2 (Ono 1998; 2007), are taken into account. Thus, the phase transformation between coesite and coesite-II may offer a new possibility for the interpretation of seismic low velocity observed at deep depths in cold subduction zones.

Acknowledgement

This work is supported by NSF(EAR1045630) and DOE/NNSA(DE-NA0001815). The authors thank Xinguo Hong in technical support at X17C beamline at National Synchrotron Light Source, Brookheaven National Laboratory. X17C is supported by COMPRES under NSF Cooperative Aggrement EAR 06-49658. MPI publication number 506.

Reference

Akaogi, M., and Navrotsky, A. (1984) The quartz-coesite-stishovite transformations: new calorimetric measurements and calculation of phase diagrams." Physics of the Earth and Planetary Interiors, 36, 124-134.

Akaogi, M., Yusa, H., Shiraishi, K., and Suzuki, T. (1995) Thermodynamic properties of α-quartz, coesite, and stishovite and equilibrium phase relations at high pressures and high temperatures." Journal of Geophysical Research: Solid Earth (1978–2012) 100, 22337-22347.

Angel, R.J., Mosenfelder, J.L., and Shaw, C.S.J. (2001) Anomalous compression and equation of state of coesite. Physics of the Earth and Planetary Interiors, 124, 71-79.

Birch, F. (1978) Finite strain isotherm and velocities for single-crystal and polycrystalline NaCl at high pressures and 300 K. Journal of Geophysical Research: Solid Earth (1978–2012) 83, 1257-1268.

Carpenter, M.A., Salje, E.K.H., and Graeme-Barber, A. (1998) Spontaneous strain as a determinant of thermodynamic properties for phase transformations in minerals. European Journal of Mineralogy, 10, 621-691.

Ceperley, D.M., and Alder, B.J. (1980) Ground state of the electron gas by a stochastic method. Physical Review Letters, 45, 566.

Černok, A., Ballaran, T.B., Caracas, R., Miyajima, N., Bykova, E., Prakapenka, V., Liermann, H.P., and Dubrovinsky, L. (2014a) Pressure-induced phase transitions in coesite. American Mineralogist , 99, 755-763.

Černok, A., Bykova, E., Ballaran, T.B., Liermann, H.P., Hanfland, M., and Dubrovinsky, L. (2014b) High-pressure crystal chemistry of coesite-I and its transition to coesite-II. Zeitschrift für Kristallographie-Crystalline Materials, 229, 761-773.

Chen, T., Gwanmesia, G.D., Wang, X., Zou, Y., Liebermann, R.C., Michaut, C., and Li, B. (2015) Anomalous elastic properties of coesite at high pressure and implications for the upper mantle X-discontinuity. Earth and Planetary Science Letters, 412, 42-51.

Davies, G.F., and Dziewonski, A.M. (1975) Homogeneity and constitution of the Earth's lower mantle and outer core. Physics of the Earth and Planetary Interiors, 10, 336-343.

Gibbs, G.V., Boisen, M.B., Rosso, K.M., Teter, D.M., and Bukowinski, M.S.T. (2000) Model structures and electron density distributions for the silica polymorph coesite at pressure: an assessment of OO bonded interactions. The Journal of Physical Chemistry B, 104, 10534-10542.

Hammersley, A.P., Svensson, S.O., Hanfland, M., Fitch, A.N., and Hausermann, D. (1996) Two-dimensional detector software: from real detector to idealised image or two-theta scan. International Journal of High Pressure Research, 14, 235-248.

Hemley, R.J. (1987) Pressure dependence of Raman spectra of SiO2 polymorphs: α-quartz, coesite, and stishovite. High Pressure Research in Mineral Physics, 39, 347-359

Hemley, R.J., Jephcoat, A.P., Mao, H.K., Ming, L.C., and Manghnani, M.H. (1988) Pressure-induced amorphization of crystalline silica. Nature, 334, 52-54.

Hu, Q.Y., Shu, J.F., Cadien, A., Meng, Y., Yang, W.G., Sheng, H.W., and Mao, H.K. (2015) Polymorphic phase transition mechanism of compressed coesite. Nature communications, 6.

Irifune, T., and Tsuchiya, T. (2007) Mineralogy of the Earth—Phase transitions and mineralogy of the lower mantle. Treatise on geophysics, 2, 33-62.

Karki, B.B., Warren, M.C., Stixrude, L., Ackland, G.J., and Crain, J. (1997a) Ab initio studies of high-pressure structural transformations in silica. Physical Review B, 55, 3465-3472.

Karki, B.B., Stixrude, L., and Crain, J. (1997b) Ab initio elasticity of three high-pressure polymorphs of silica. Geophysical Research Letters, 24, 3269-3272.

Kimizuka, H., Ogata, S., and Li, J. (2008) Hydrostatic compression and high-pressure elastic constants of coesite silica. Journal of Applied Physics, 103, 053506.

Klotz, S., Paumier, L., Le March, G., and Munsch, P. (2009) The effect of temperature on the hydrostatic limit of 4: 1 methanol–ethanol under pressure. High Pressure Research 29, 649-652.

Larson, A.C., and Von Dreele, R.B. (2004) General Structure Analysis System (GSAS) (Los Alamos National Laboratory, Los Alamo, NM), report no LAUR 86-748.

Levien, L., and Prewitt, C.T. (1981) High-pressure crystal structure and compressibility of coesite. American Mineralogist, 66, 324-333.

Mao, H.K., Xu, J., and Bell, P.M. (1986). Calibration of the ruby pressure gauge to 800 kbar under quasi-hydrostatic conditions. Journal of Geophysical Research, 91, 4673-4676.

Oganov, A.R., and Ono, S. (2004). Theoretical and experimental evidence for a post-perovskite phase of $MgSiO_3$ in Earth's D ″layer. Nature, 430, 445-448.

Ono, S. (1998) Stability limits of hydrous minerals in sediment and mid-ocean ridge basalt compositions: implications for water transport in subduction zones. Journal of Geophysical Research, 103, 18253–18267.

Ono, S. (2007) The Lehmann discontinuity due to dehydration of subducted sediment. The Open Mineralogy Journal, 1, 1–4.

Perdew, J.P., Burke, K., and Ernzerhof, M. (1996) Generalized gradient approximation made simple. Physical Review Letters, 77, 3865.

Perdew, J.P., and Zunger A. (1981) Self-interaction correction to density-functional approximations for many-electron systems. Physical Review B, 23, 5048.

Ricard, Y., Mattern, E., Matas, J. (2005) Synthetic tomographic images of slabs from mineral physics. In: van der Hilst, R.D., Bass, J.D., Matas, J., Trampert, J. (Eds.), Earth's Deep Mantle: Structure, Composition and Evolution. AGU, Washington, DC, pp. 283–300.

Sobolev, N.V., Fursenko, B.A., Goryainov, S.V., Shu, J., Hemley, R.J., Mao, H.K., and Boyd, F.R. (2000) Fossilized high pressure from the Earth's deep interior: The coesite-in-diamond barometer. Proceedings of the National Academy of Sciences, 97, 11875-11879.

Stixrude, L., and Lithgow-Bertelloni, C. (2012) Geophysics of chemical heterogeneity in the mantle. Annual Review of Earth and Planetary Sciences, 40, 569-595.

Toby, B.H. (2001) EXPGUI, a graphical user interface for GSAS. Journal of Applied Crystallography, 34, 210–213.

Williams, Q., and Revenaugh, J. (2005) Ancient subduction, mantle eclogite, and the 300 km seismic discontinuity. Geology, 33, 1-4.

Zhang, J., Li, B., Utsumi, W., and Liebermann, R.C. (1996) In situ X-ray observations of the coesite-stishovite transition: reversed phase boundary and kinetics. Physics and Chemistry of Minerals, 23, 1-10.

Zhang, Jin S., Bruno Reynard, Gilles Montagnac, and Jay D. Bass (2014) Pressure-induced Pbca–$P2_1/c$ phase transition of natural orthoenstatite: The effect of high temperature and its geophysical implications. Physics of the Earth and Planetary Interiors, 228, 150-159.

Figure and Table Captions:

Fig. 1. Comparison of the relative enthalpy per atom between coesite and coesite-II, stishovite.

Fig. 2. Selected X-ray diffraction patterns of coesite. The experimental patterns are aligned with the gap proportional to the pressure difference. A group of peaks from coesite-II are enlarged in the upper right figure. Besides the peaks from coesite, the bcc-Fe (110) as

well as the hcp-Fe (101) (002) (011) are also observed in the experiment. Black dashed lines show the shift of the peaks grouped around 2θ~7.5-8° with pressure.

Fig. 3. Comparison of unit cell volumes of coesite and coesite-II ($V/2$) as a function of pressure. Results from GGA calculations were adjusted by applying a correction of -3.6 GPa to pressures. The refined results obtained from this study for coesite are consistent with single crystal studies by Angel et al. (2001), as well as by Levien and Prewitt (1981) [not plotted in Fig. 3 for clarity].

Fig. 4. Compressibility of unit cell parameters. Results from the current GGA calculations were applied a correction of -3.6 GPa to pressures.

Fig. 5. Compression of (a) Si-O bonds in coesite and the evolution of the shortest Si1-O1 (b) the five Si-O-Si angles in coesite and the evolution of the linear Si1-O1-Si1 angle above the phase transition in coesite-II. The current calculations were adjusted by applying a correction of -3.6 GPa to pressures.

Fig 6. Structure of coesite and coesite-II at 21.4 GPa from DFT calculations. A and C: polyhedral illustration of the silica tetrahedral for coesite and coesite-II at 21.4 GPa respectively viewed down the *b*-axis. B and D: illustration of the Si1-O1-Si1 angle in coesite and its evolved angles Si5-O4-Si7 and Si2-O15-Si3 in coesite-II viewed down the *a*-axis (circled out in A and C).

Table 1. Cell parameters and unit cell volumes from diamond anvil cell experiments and DFT (GGA) calculations

Table 2. Comparison of bulk modulus for coesite and coesite-II in this study with previous results

Table 3. Axial bulk modulus of coesite and coesite-II

This is a preprint, the final version is subject to change, of the American Mineralogist (MSA)
Cite as Authors (Year) Title. American Mineralogist, in press.
(DOI will not work until issue is live.) DOI: http://dx.doi.org/10.2138/am-2016-5533

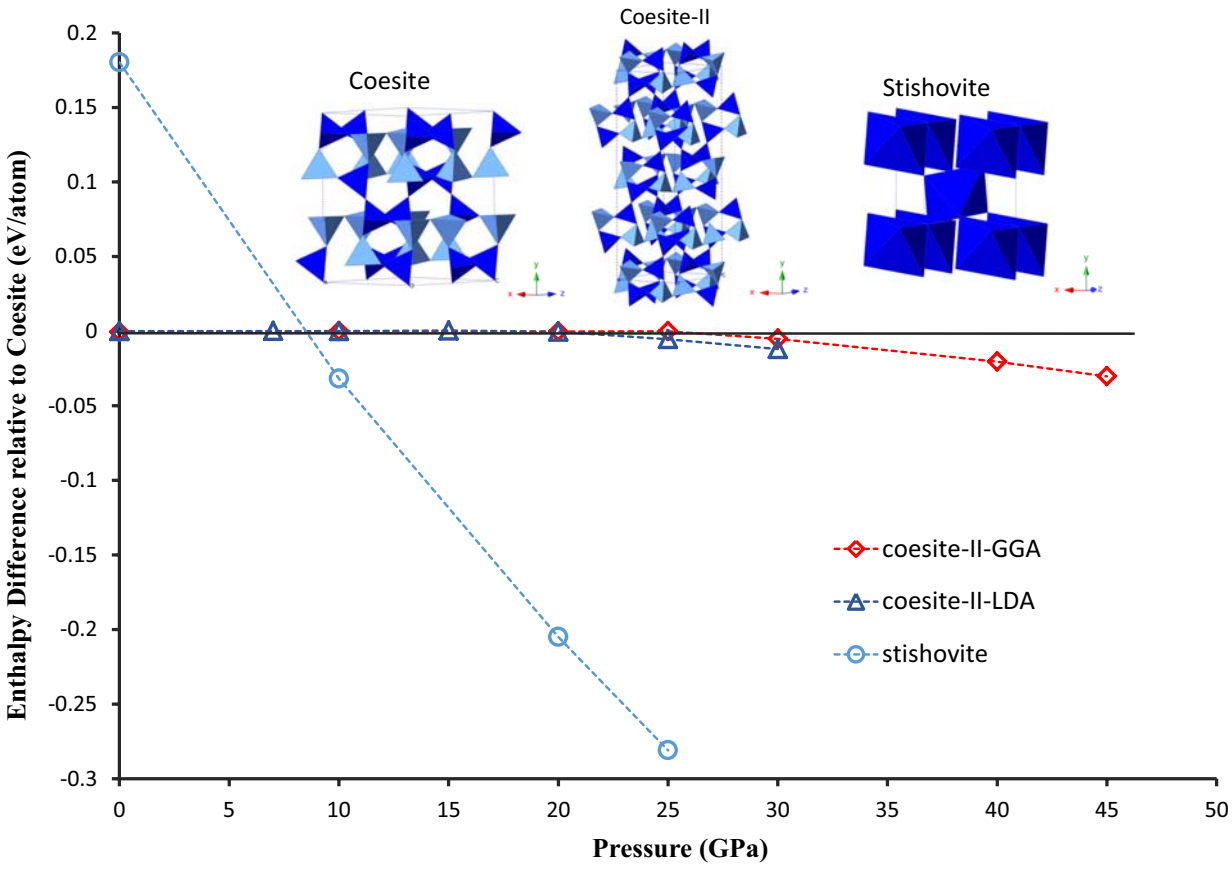

Fig.1

This is a preprint, the final version is subject to change, of the American Mineralogist (MSA)
Cite as Authors (Year) Title. American Mineralogist, in press.
(DOI will not work until issue is live.) DOI: http://dx.doi.org/10.2138/am-2016-5533

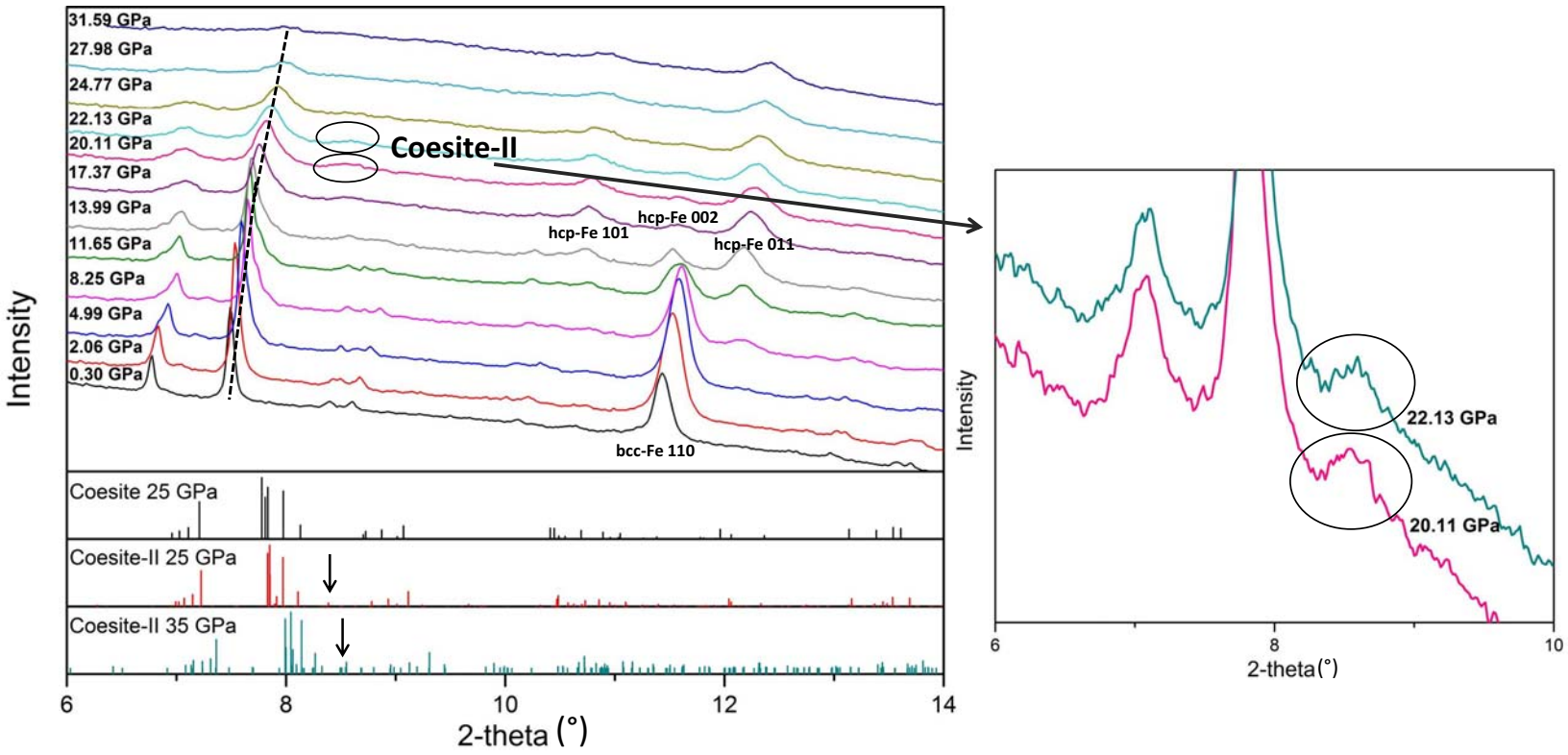

Fig.2

This is a preprint, the final version is subject to change, of the American Mineralogist (MSA)
Cite as Authors (Year) Title. American Mineralogist, in press.
(DOI will not work until issue is live.) DOI: http://dx.doi.org/10.2138/am-2016-5533

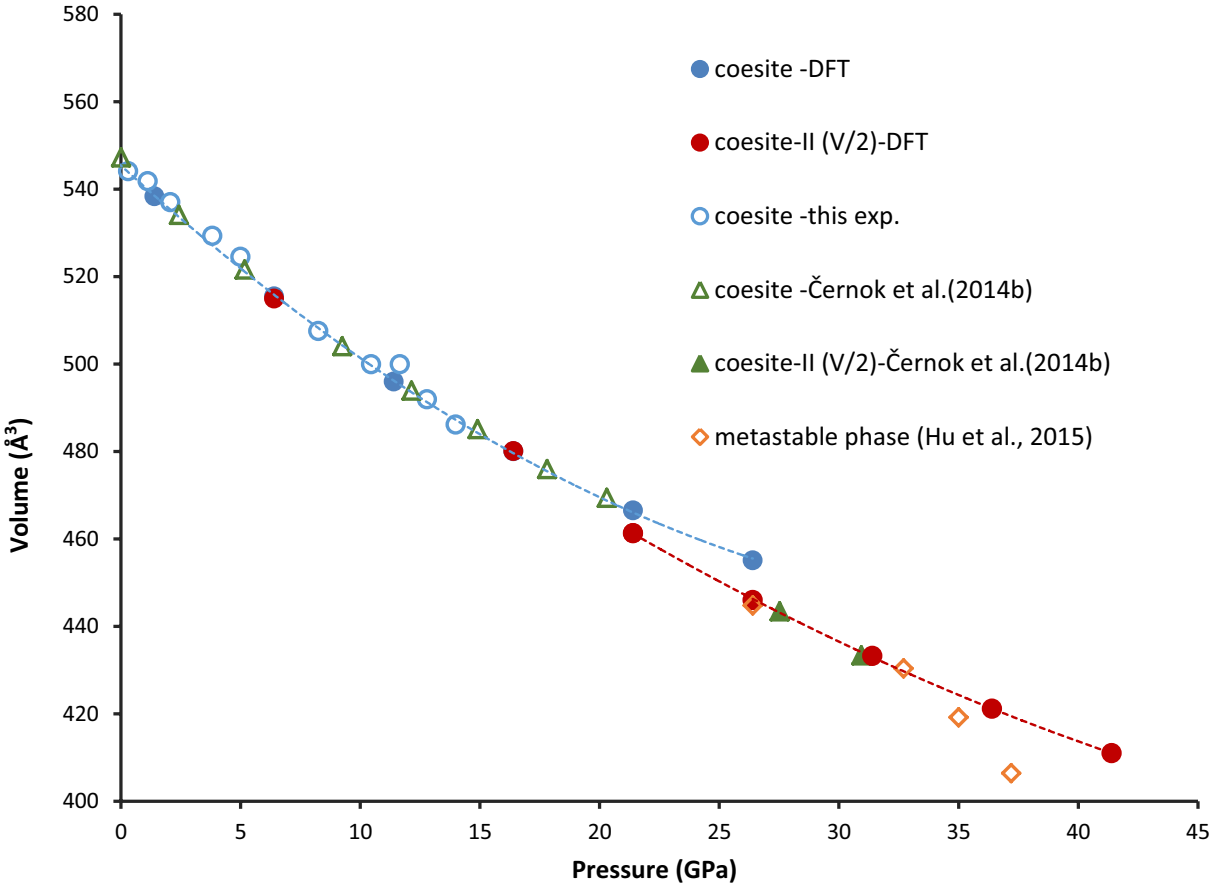

Fig.3

This is a preprint, the final version is subject to change, of the American Mineralogist (MSA)
Cite as Authors (Year) Title. American Mineralogist, in press.
(DOI will not work until issue is live.) DOI: http://dx.doi.org/10.2138/am-2016-5533

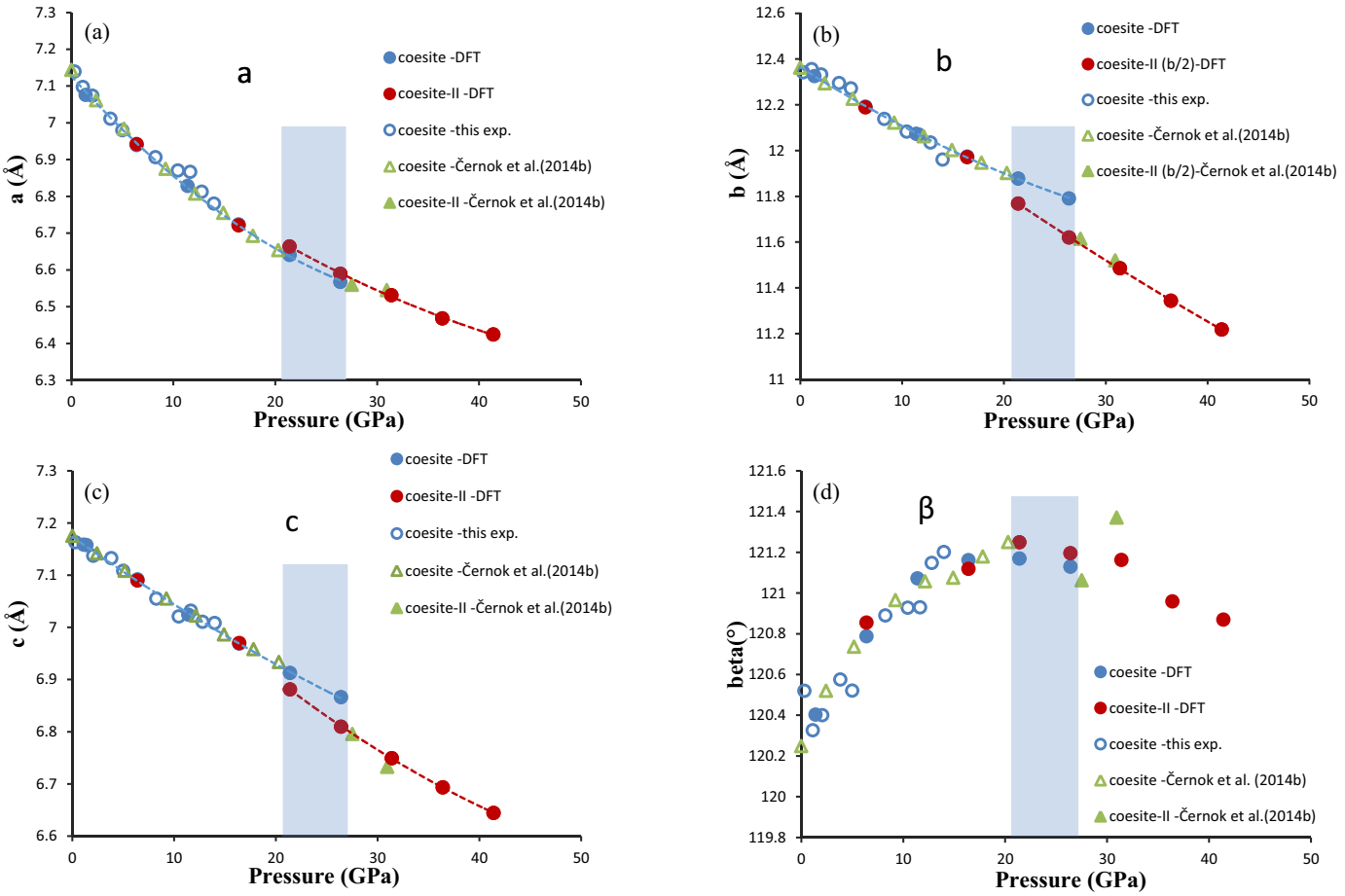

Fig.4

This is a preprint, the final version is subject to change, of the American Mineralogist (MSA)
Cite as Authors (Year) Title. American Mineralogist, in press.
(DOI will not work until issue is live.) DOI: http://dx.doi.org/10.2138/am-2016-5533

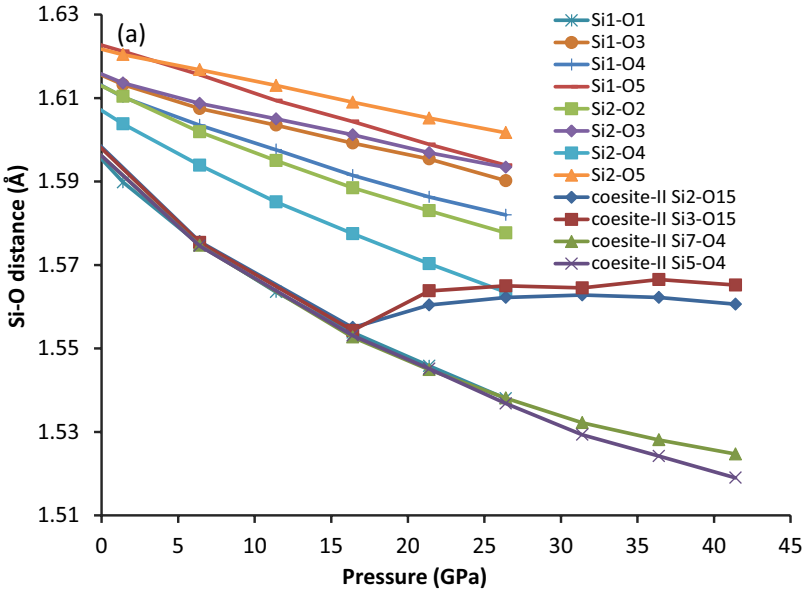

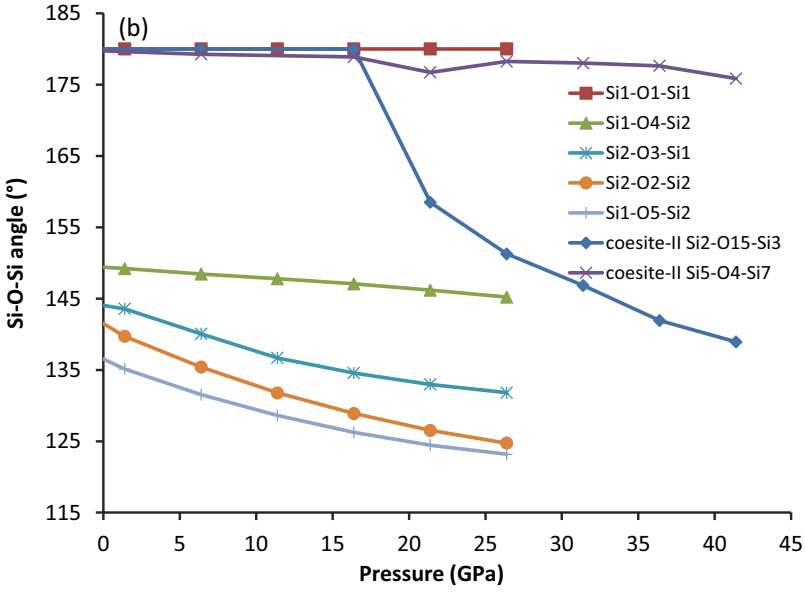

Fig.5

This is a preprint, the final version is subject to change, of the American Mineralogist (MSA)
Cite as Authors (Year) Title. American Mineralogist, in press.
(DOI will not work until issue is live.) DOI: http://dx.doi.org/10.2138/am-2016-5533

Coesite (C2/c)
21.4 GPa

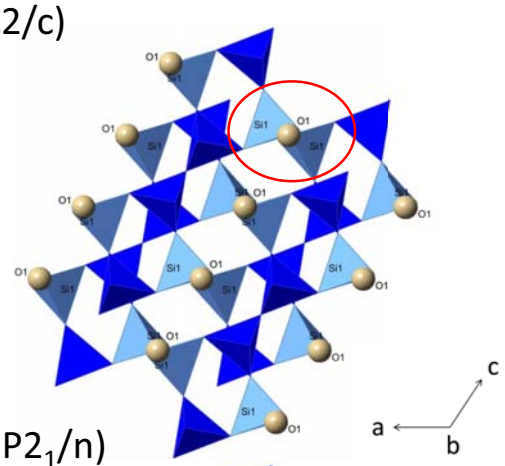

A

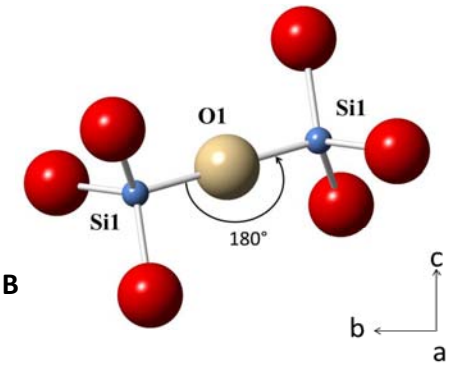

B

Coesite-II ($P2_1/n$)
21.4 GPa

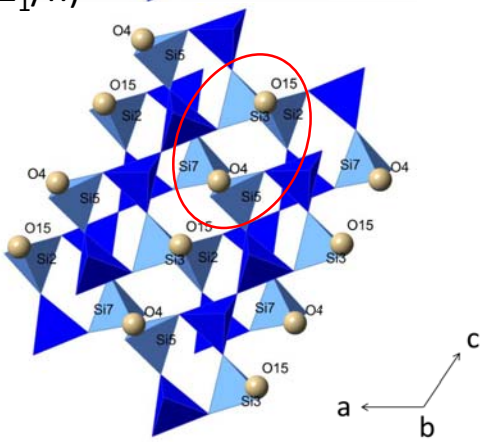

C

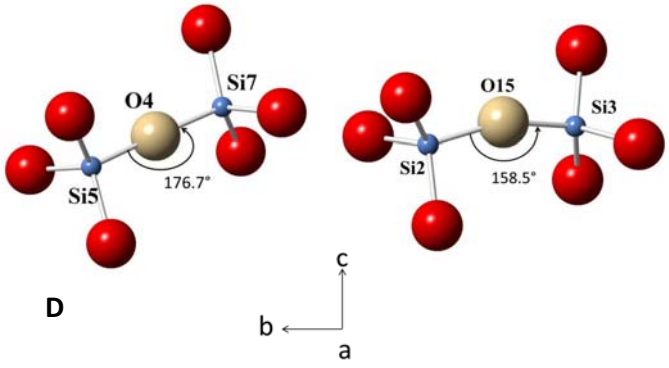

D

Fig.6

This is a preprint, the final version is subject to change, of the American Mineralogist (MSA)
Cite as Authors (Year) Title. American Mineralogist, in press.
(DOI will not work until issue is live.) DOI: http://dx.doi.org/10.2138/am-2016-5533

Table 1. Cell parameters and unit cell volumes from diamond anvil cell experiments and DFT (GGA) calculations

P (GPa)	*a* (Å)	*b* (Å)	*c* (Å)	beta(°)	*V* (Å^3)
Coesite -DAC experiments					
0.30	7.139(2)	12.342(1)	7.163(2)	120.52(1)	543.7(1)
1.12	7.097(2)	12.355(8)	7.158(2)	120.33(1)	541.8(3)
2.06	7.074(4)	12.332(8)	7.137(4)	120.40(1)	537.0(8)
3.82	7.011(6)	12.295(8)	7.132(5)	120.58(1)	529.3(9)
4.99	6.980(2)	12.272(2)	7.108(1)	120.52(1)	524.5(1)
8.25	6.906(2)	12.138(4)	7.055(2)	120.89(1)	507.6(0)
10.45	6.870(2)	12.083(7)	7.021(3)	120.93(2)	499.9(1)
11.65	6.866(1)	12.070(3)	7.032(2)	120.93(1)	499.9(0)
12.79	6.812(2)	12.035(6)	7.011(1)	121.15(2)	491.9(2)
13.99	6.780(1)	11.961(3)	7.008(1)	121.20(2)	486.1(1)
Coesite –DFT calculations					
0	7.2493	12.4696	7.2215	120.149	564.49
5	7.0755	12.3251	7.1575	120.403	538.35
10	6.9395	12.1919	7.0919	120.787	515.46
15	6.8280	12.0734	7.0241	121.072	495.96
20	6.7234	11.9735	6.9686	121.161	480.05
25	6.6408	11.8773	6.9126	121.169	466.52
30	6.5670	11.7910	6.8660	121.129	455.09
Coesite-II –DFT calculations					
0	7.2426	24.9784	7.2218	120.006	1131.38
10	6.9421	24.3766	7.0895	120.855	1029.92
20	6.7209	23.9418	6.9699	121.118	960.15
25	6.6637	23.5357	6.8809	121.249	922.60
30	6.5894	23.2399	6.8095	121.195	892.01
35	6.5309	22.9705	6.7492	121.162	866.41
40	6.4679	22.6874	6.6934	120.959	842.26
45	6.4243	22.4358	6.6443	120.869	822.01

Table 2. Comparison of bulk modulus for coesite and coesite-II in this study with previous results

	K_0(GPa)	K_0'	Max P (GPa)	Reference
Coesite(C2/c, room P)	96.2	4.3	25(21.4 after correction)	DFT calculations-This study
	106.2	2.1	13.99	DAC experiment-This study
	96	8.4	5.19	Levien and Prewitt (1981)
	100.8	1.8	9.6	Angel et al. (2001)
	114	8[a]	8.5	Bassett and Barnett (1970)
	126	4[a]		
	95.9	-	15	[b]Kimizuka et al. (2008)
Coesite-II($P2_1/n$, 21.4 GPa)	140.8	3.58	45(41.4 after correction)	DFT calculations-This study

[a]assumed, [b]DFT calculations

Table 3. Axial bulk modulus of coesite and coesite-II

	K_a(GPa)	K_a'	K_b(GPa)	K_b'	K_c(GPa)	K_c'	Reference
Coesite(C2/c, room P)	73.2	3.25	142.7	3.74	175.5	1.82	DFT calculations-This study
	76.0	2.99	144.6	0	158.2	4.59	DAC experiment-This study
	66.3[*]	3.4[*]	143	3.6	173	2.5	Černok et al. (2014b)
Coesite-II($P2_1/n$, 21.4 GPa)	138.9	4.77	129.4	1.42	150.6	4.47	DFT calculations-This study

[*]calculated using unit cell parameters from Černok et al. (2014b)

Axial compressibility $= \frac{1}{3K_x}$, x=a, b, c